

# Theory of Polymer–Nanopore Interactions Refined Using Molecular Dynamics Simulations

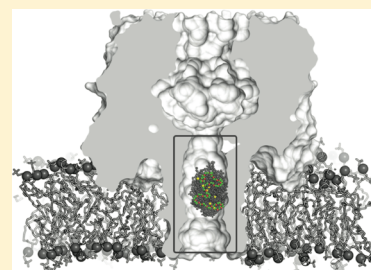
Arvind Balijepalli,<sup>†,‡</sup> Joseph W. F. Robertson,<sup>‡</sup> Joseph E. Reiner,<sup>§</sup> John J. Kasianowicz,<sup>‡</sup> and Richard W. Pastor<sup>\*,†</sup>

<sup>†</sup>National Heart, Lung, and Blood Institute, National Institutes of Health, Bethesda, Maryland 20892, United States

<sup>‡</sup>Physical Measurement Laboratory, National Institute of Standards and Technology, Gaithersburg, Maryland 20899, United States

<sup>§</sup>Department of Physics, Virginia Commonwealth University, Richmond, Virginia 23220, United States

**ABSTRACT:** Molecular dynamics simulations were used to refine a theoretical model that describes the interaction of single polyethylene glycol (PEG) molecules with  $\alpha$ -hemolysin ( $\alpha$ HL) nanopores. The simulations support the underlying assumptions of the model, that PEG decreases the pore conductance by binding cations (which reduces the number of mobile ions in the pore) and by volume exclusion, and provide bounds for fits to new experimental data. Estimation of cation binding indicates that four monomers coordinate a single  $K^+$  in a crown-ether-like structure, with, on average, 1.5 cations bound to a PEG 29-mer at a bulk electrolyte concentration of 4 M KCl. Additionally, PEG is more cylindrical and has a larger cross-section area in the pore than in solution, although its volume is similar. Two key experimental quantities of PEG are described by the model: the ratio of single channel current in the presence of PEG to that in the polymer's absence (blockade depth) and the mean residence time of PEG in the pore. The refined theoretical model is simultaneously fit to the experimentally determined current blockade depth and the mean residence times for PEGs with 15 to 45 monomers, at applied transmembrane potentials of  $-40$  to  $-80$  mV and for three electrolyte concentrations. The model estimates the free energy of the PEG–cation complexes to be  $-5.3 k_B T$ . Finally the entropic penalty of confining PEG to the pore is found to be inversely proportional to the electrolyte concentration.



## INTRODUCTION

Biological nanopores have been used to electrically detect and characterize molecules, thereby enabling a wide range of sensing applications.<sup>1–3</sup> This technology is possible because the pores have dimensions that are commensurate with single molecules,<sup>4</sup> do not gate,<sup>5</sup> and retain molecules in the pore far longer than would be expected for freely diffusing species.<sup>6</sup> Protein nanopores have been used to detect many analyte types including  $H^+$  and  $D^+$  ions in solution,<sup>5,7</sup> DNA and RNA polynucleotides,<sup>8–14</sup> therapeutic agents against anthrax toxins,<sup>1,3,15,16</sup> proteins,<sup>17,18</sup> polypeptides,<sup>19</sup> polyethylene glycol (PEG),<sup>6,20–24</sup> and synthetic molecules.<sup>23–27</sup> Recently, the *Staphylococcus aureus*  $\alpha$ -hemolysin ( $\alpha$ HL) nanopore was used to discriminate between different size polymers, which provides the basis for a form of single molecule mass spectrometry (SMMS).<sup>23,24</sup>

There has been considerable interest in the use of single nanopores to sequence DNA.<sup>1,8,28–32</sup> However, the method remains elusive, in part because it has been difficult to discern small differences between the four DNA mononucleotides to better than  $2\sigma$  on average.<sup>33</sup> The SMMS technique noted above provides the basis for a nanopore-based DNA sequencing by synthesis (SBS) approach, because polymeric tags can be used as surrogates for mononucleotides and detected by the nanopore with  $>6\sigma$  separation.<sup>34</sup> The ability to use PEG and PEG analogs for this and other applications demands a

physically accurate description of their interactions with nanopores.

Here, we use molecular dynamics (MD) simulations to critically test and refine a theoretical model<sup>24</sup> that quantifies the interactions between single PEG molecules in the  $\alpha$ HL pore (Figure 1). The model assumes that PEG decreases the pore conductance by two physical processes: (i) volume exclusion due to the presence of the polymer in the pore and (ii) a decrease in the mobile ion concentration due to the formation of reversible PEG–cation complexes. Newly obtained experimental data measured over a wide range of PEG molecular weights, electrolyte concentrations, and transmembrane potentials are then fit to the refined theoretical model, which leads to a better estimation of the model parameters. The techniques reported here provide the basis to analyze a variety of molecules, for example, labels that can be used in nanopore-based DNA sequencing.<sup>34</sup>

## MATERIALS AND METHODS

**MD Simulation.** All simulations were performed using NAMD 2.8<sup>36</sup> and the analyses were performed using CHARMM c36b2.<sup>37</sup> Force field parameters were from CHARMM and obtained by combining protein parameters from C22 with the CMAP correction,<sup>38,39</sup> ether parameters from C35r,<sup>40</sup> lipid parameters from

Received: March 13, 2013

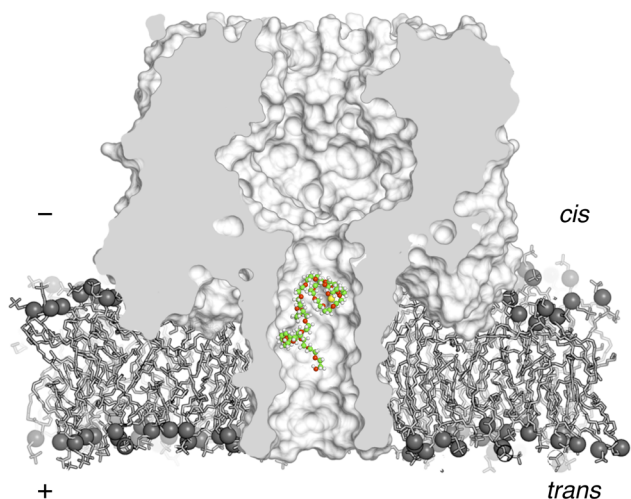


**Figure 1.** Cross-section of an  $\alpha$ HL nanopore in a lipid bilayer. The pore has two major components: the cap region on the *cis* side with a relatively large vestibule, and the narrower stem portion spanning the membrane that is used in single molecule sensing applications. An electrostatic potential, applied relative the *trans* side of the pore to match experiment drives an ionic current across the channel. PEG partitions into the narrow stem region on the *trans* side, thereby blocking the pore. In the size range studied as part of this work, PEG molecules decrease the channel conductance proportional to their size. In contrast, the mean residence time of PEG increases with the size of the molecule. This image was created with PyMol.<sup>35</sup>

C36,<sup>41</sup> and the TIP3P water model.<sup>42</sup> Pressure control with a Nosé-Hoover Langevin piston<sup>43,44</sup> was used to maintain a pressure of 1 atm during initial equilibration. Temperature was maintained by coupling the system to a Langevin bath with a damping frequency of  $1 \text{ ps}^{-1}$ . Electrostatic forces were calculated using particle mesh Ewald summation<sup>45</sup> with a real space cutoff of 12 Å. Lennard-Jones forces were switched smoothly to zero between 10 and 12 Å. Simulations were performed with a 2 fs time step, and coordinates were saved at 2 ps intervals. SHAKE was used to constrain the hydrogen-carbon bonds.<sup>46</sup>

Simulations of a single PEG29 molecule in bulk solution were performed using a cubic periodic simulation cell with edge length 50 Å. Four simulation systems consisting of 3797, 3786, 3526, and 3394 TIP3P water molecules and 0, 69, 206, 275 pairs of  $\text{K}^+$  and  $\text{Cl}^-$  ions were setup to yield electrolyte concentrations of  $\approx 0, 1, 3,$  and  $4 \text{ M}$ , respectively. One thousand steps of energy minimization were performed, followed by heating the simulation cell from 200 K to a final temperature of 293 K. After 5 ns of equilibration under a constant isotropic pressure (NPT) of 1 atm, the edge length of each simulation cell converged to 48.5, 48.9, 48.6, and 48.5 Å, respectively, for each of the four electrolyte concentrations. After equilibration, pressure control was turned off, and the simulations were run under constant volume and constant temperature (NVT) to generate 100 ns trajectories from which average properties were calculated.

Nanopore simulations were setup using CHARMM-GUI.<sup>47</sup> A single  $\alpha$ HL nanopore was incorporated in a square patch of 1-palmitoyl-2-oleoyl-*sn*-glycero-3-phosphocholine (POPC) lipid bilayer with an edge length of 120.25 Å. The system includes 344 lipids, 41 106 TIP3P water molecules, and 3169 pairs of  $\text{K}^+$  and  $\text{Cl}^-$  ions, with an additional 7  $\text{Cl}^-$  counterions to yield a system that was electrostatically neutral. The system was initially run under NPT conditions to allow the bilayer to equilibrate. Additional equilibration for 10 ns was then performed by fixing the bilayer area and maintaining the pressure normal to the bilayer at 1 atm (NPAT). During this stage the simulation cell was heated to a final temperature of 293 K. The final height of the simulation cell after equilibration was 144.57 Å, and the final electrolyte concentration was 4 M KCl. After equilibration, the simulations were run under NVT conditions, and a transmembrane

potential of  $-40 \text{ mV}$  was applied with the *trans* side at ground (Figure 1). One 250 ns trajectory was generated in the absence of PEG in the nanopore. Two 500 ns trajectories were generated, each with a single PEG29 placed in the transmembrane region of the pore. Ten shorter trajectories (50 ns each) were initialized with snapshots from the two long simulations to yield an additional 500 ns. Lastly, two 100 ns trajectories at electrolyte concentrations of 3 and 3.5 M KCl were generated using the same initial conditions as the 4 M KCl simulations to obtain a total of 1.7  $\mu\text{s}$  for PEG in  $\alpha$ HL.

**Single-Molecule Nanopore Experiments.** Planar solvent-free lipid bilayers were formed with 1,2 diphytanoyl-*sn*-glycero-3-phosphatidylcholine (DPhyPC) in *n*-decane on quartz capillaries.<sup>48</sup> The capillary used in this study had an aperture with a diameter of 1.04  $\mu\text{m}$ . The capillary was filled with a mixture of heterogeneous distributions of PEG: 30  $\mu\text{M}$  of each 1000 and 1500 g/mol, and a calibration standard consisting of 1  $\mu\text{M}$  of highly purified PEG29,  $M_w = 1251 \text{ g/mol}$ . PEG was dissolved in either 3 M, 3.5 M, or 4 M KCl, each buffered with 10 mM tris and titrated with 3 M citric acid to pH 7.2. The capillary was first immersed in electrolyte solution (with the same ionic strength as the solution inside the capillary but with no added PEG), and a pipet tip was used to paint the capillary face with a solution of DPhyPC in *n*-decane to spontaneously form a membrane. After  $\approx 10 \text{ min}$ , 0.5  $\mu\text{L}$  of  $\alpha$ HL (0.5 mg/mL) was added to the external solution bath. A pressure of 80 to 140 mmHg on the capillary side was used to decrease the membrane thickness and aid in channel incorporation. Once a single channel was incorporated into the membrane, the pressure was reduced to  $\approx 40 \text{ mmHg}$  to prevent further channel formation. The measurement was performed at applied transmembrane potentials varying between  $-40 \text{ mV}$  and  $-80 \text{ mV}$  for each electrolyte concentration. Data were sampled at 500 kHz after being filtered with an 8-pole Bessel filter with a cutoff frequency of 100 kHz.

**Theory of PEG in an  $\alpha$ HL Nanopore.** We refine an analytical model that describes the interactions of PEG with an  $\alpha$ HL nanopore.<sup>24</sup> Specifically, the model describes the decrease in channel conductance and the mean residence time, due to the presence of PEG in the pore. The model assumes PEG decreases the ionic current measured across the pore by two physical processes: volume exclusion and reversible PEG-cation complexes. Ignoring molecular fluctuations, PEG was represented by a charged cylinder with cross-sectional area  $A_{\text{PEG}}$  and length  $L_{\text{PEG}}$ . Further, the model assumed that PEG is confined to the transmembrane region of the pore, represented by a cylinder of area  $A_{\text{pore}}$  and length  $L_{\text{pore}}$ . The expression for the blockade depth (see Reiner et al.<sup>24</sup> for a detailed derivation), defined as the ratio of the average ionic current when PEG is present in the pore ( $\langle i \rangle$ ) to the average ionic current across an empty channel ( $\langle i_0 \rangle$ ), is

$$\frac{\langle i \rangle}{\langle i_0 \rangle} = \left( 1 - \frac{L_{\text{PEG}}}{L_{\text{pore}}} \left( 1 - \frac{2}{\left( a^* - b \frac{m_{\text{B}}}{m_{\text{T}}} \right) \left( 1 - \frac{A_{\text{PEG}}}{A_{\text{pore}}} \right)} \right) \right)^{-1} \quad (1)$$

where  $a^* = (\delta_{+}^{\text{eff}} + \delta_{-}^{\text{eff}})/D_{\text{p}}$ ,  $b^* = \delta_{+}^{\text{eff}}/D_{\text{p}}$ ,  $\delta_{+}^{\text{eff}}$  and  $\delta_{-}^{\text{eff}}$  are concentration-weighted diffusion constants of cations and anions inside the pore, and  $D_{\text{p}}$  is the diffusion constant of ions in the pore, in the absence of PEG. The blockade depth also depends on the number of cations inside the pore,  $m_{\text{T}} = C_{\text{p}} L_{\text{PEG}} (A_{\text{pore}} - A_{\text{PEG}})$ , where  $C_{\text{p}}$  is the KCl concentration inside the pore in the presence of PEG. The number of cations bound to the PEG is given by

$$m_{\text{B}} = \frac{\alpha - \sqrt{\alpha^2 - 4m_{\text{T}}nr_{\text{m}}^+}}{2} \quad (2)$$

where  $n$  is the number of monomers in the PEG,  $r_{\text{m}}^+$  is the average number of monomers in the chain for each bound cation,  $\alpha = m_{\text{T}} + nr_{\text{m}}^+ K_{\text{A}}^{-1}$ , with an association constant  $K_{\text{A}} = \exp(-\beta(\Delta G_{\text{pore}} + s^+ eV_{\text{app}}))$ . Finally,  $\Delta G_{\text{pore}}$  is the free energy change associated with PEG binding a single cation (Figure 2),  $\beta$  is the thermal energy,  $e$  is the electron charge,  $V_{\text{app}}$  is the applied transmembrane potential, and  $s^+$  is a freely

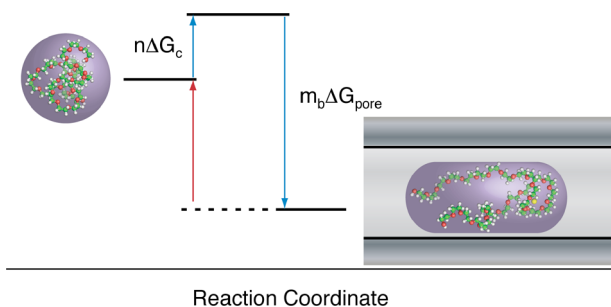


**Figure 2.** Kinetics of PEG partitioning into the nanopore is described by reversible reactions. PEG kinetics contribute to a description of both the channel conductance and the mean residence time. In order to enter the pore (blue arrows), PEG must overcome an entropic barrier ( $n\Delta G_c$ ). The model also accounts for reversible PEG–cation complexes, formed when PEG adsorbs  $m_B$  cations resulting in a free energy change of  $m_B\Delta G_{\text{pore}}$ . In addition to volume exclusion, the adsorbed ions decrease the local ion concentration and further reduce the channel conductance. The mean residence time of PEG is determined by the free energy of dissociation. PEG exits the pore when  $m_B$  cations dissociate from the complex (red arrow) and follows a single exponential distribution.

adjustable parameter that balances the electroosmotic and electrophoretic forces acting on a single cation.

The mean residence time  $\langle\tau_n\rangle$  of PEG is determined by the free energy of dissociation of the molecule from the nanopore and is expressed using the Arrhenius rate equation:

$$\langle\tau_n\rangle = \frac{\xi\epsilon L_{\text{PEG}}}{m_B|V_{\text{app}}|} \exp(-\beta(n\Delta G_c + m_B(\Delta G_{\text{pore}} + s^{\text{PEG}}e|V_{\text{app}}|))) \quad (3)$$

where  $\Delta G_c$  is the free energy change per monomer associated with confining PEG to the nanopore,  $\xi$  is the hydrodynamic drag acting on PEG, and  $s^{\text{PEG}} = \gamma(1 - F_V^{\text{PEG}}/F_E^{\text{PEG}})$  is an adjustable parameter that balances the electroosmotic and electrophoretic forces ( $F_V^{\text{PEG}}/F_E^{\text{PEG}}$ ) acting on PEG inside the pore.

## RESULTS AND DISCUSSION

**Ionic Current.** Ionic currents were calculated from trajectories for a pore in the absence (unblocked) and presence of a single PEG molecule. Assuming the channel conductance is ohmic,<sup>49</sup> the ionic current is  $i = (N_{\text{K}^+} - N_{\text{Cl}^-})q/\Delta t$ , where  $N_{\text{K}^+}$  and  $N_{\text{Cl}^-}$  are the accumulated crossings of each ionic species

across the channel,  $q$  is the charge of the ion, and  $\Delta t$  is the time interval of the measurement. The ionic current was calculated across a transverse plane at the geometric center of the membrane, from each saved frame of the trajectory (Figure 3 left, inset and Table 1). For the unblocked pore, the magnitude

**Table 1. Mean Ionic Currents (4 M KCl and  $-40$  mV applied potential)**

	$\langle i \rangle$ (pA)	$\langle i_0 \rangle$ (pA)	$\langle i \rangle / \langle i_0 \rangle$
open pore	–	$119 \pm 11$	–
MD			
PEG29 T1	$21 \pm 7$	–	$0.19 \pm 0.09$
PEG29 T2	$8 \pm 4$	–	$0.07 \pm 0.05$
PEG29 T3	$26 \pm 9$	–	$0.23 \pm 0.09$
average	$19 \pm 7$	$119 \pm 11$	$0.16 \pm 0.04$
experiment <sup>23</sup>	$37 \pm 1$	$150 \pm 3$	$0.25 \pm 0.005$

of the net ionic current  $\langle i_0 \rangle = 119 \pm 11$  pA, calculated using 250 ns of simulation data at an applied transmembrane potential,  $V_{\text{app}} = -40$  mV. This value is  $\sim 20\%$  lower than the experimentally measured open channel current under identical conditions.<sup>23,50</sup> The systematic error in the simulated ionic currents can be partially attributed to the parametrization of the force field<sup>51</sup> and is comparable with other simulation studies.<sup>52–55</sup>

The ionic current with PEG present in the pore ( $\langle i \rangle$ ) was estimated from two all-atom MD simulations (PEG29 T1 and PEG29 T2), each 500 ns long and generated under the same conditions as the open pore case. In each simulation, a single PEG29 was placed in the transmembrane region of the nanopore with a random starting conformation. Figure 3 (left) shows the accumulated ion flux ( $N_{\text{K}^+} - N_{\text{Cl}^-}$ ) as a function of time for the two trajectories. At least two distinct states, delineated by the slopes of the curve, can be observed from this plot. Flat regions of the curve indicate a nonconducting state, where the molecule almost entirely blocks the pore, and regions with steeper slope ( $>0.15$  q/ns) indicate a conducting state, where the ionic current exceeds experiment.<sup>23</sup> We obtain  $\langle i \rangle$  for the trajectories by first calculating the current independently for each conducting and nonconducting segment and then performing a weighted average. Ionic currents and the average blockade depths ( $\langle i \rangle / \langle i_0 \rangle$ ) calculated from each trajectory are shown in Table 1. In the case of PEG29 T1, the average

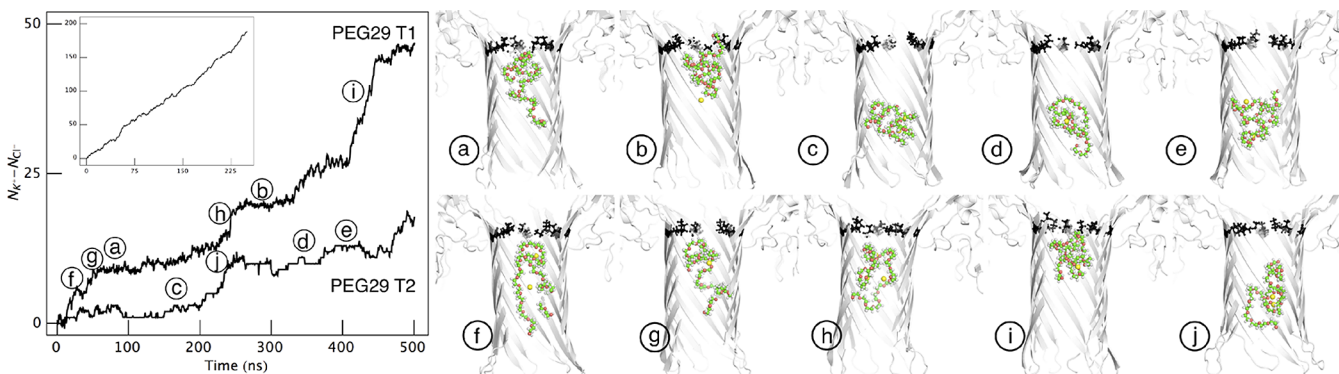


**Figure 3.** Ionic current calculations from molecular dynamics simulations of PEG in  $\alpha$ HL nanopores. (Left) Ion flux across the geometric center of the membrane, as a function of time, with no PEG blocking the pore (250 ns, inset) and two trajectories with PEG29 inside the pore (500 ns each, PEG29 T1 and PEG29 T2). (Right) Starting conformations, sampled from PEG29 T1 and PEG29 T2, for ten 50 ns long simulations are shown, where the channel was either in a nonconducting state (top row) or in a conducting state (bottom row). Only the transmembrane stem region is shown in each figure with atomic representations of Lys 147 and Glu 111 (black) to highlight the constriction in the channel.<sup>4</sup>

blockade depth is  $0.19 \pm 0.09$ , consistent with the experimental value of  $0.25 \pm 0.005$  within two standard errors.<sup>23</sup> PEG29 T2 yields a blockade depth of  $0.07 \pm 0.04$ , which is systematically lower than experiment.

To further sample PEG conformations in the nanopore, we ran 10 additional simulations (Figure 3), each 50 ns long (500 ns total, PEG29 T3), with starting PEG conformations taken equally from the conducting and nonconducting states of PEG29 T1 and PEG29 T2. Combining the ionic currents from the individual segments resulted in a combined blockade depth of  $0.23 \pm 0.09$  that is consistent with experiment. An average of all the simulations resulted in a blockade depth of  $0.16 \pm 0.04$ . The simulations demonstrate that the average ionic current is obtained from the superposition of two or more distinct states, which are too short-lived to be presently measured experimentally. Therefore, the theoretical model describes PEG interactions using the long-time average of the ionic currents to enable comparison with experiment.

**PEG Geometry.** At low molecular weights, PEG acts as an ideal chain in bulk solution.<sup>56,57</sup> The radius of gyration ( $R_g$ ) then satisfies the relationship  $R_g \propto M_w^\nu$ , where  $M_w$  is the molecular weight of the molecule and  $\nu$  is the Flory exponent, which is 0.5 for an ideal chain. This was verified for PEG in water (calculated for the  $\theta$ -condition) within statistical error using MD simulations.<sup>40</sup> In contrast, PEG coordinates cations in electrolyte solution form compact helical crown ether-like structures.<sup>58</sup> The number of ions bound to the chain scales directly with electrolyte concentration and consequently PEG takes on more compact conformations. Small angle neutron scattering (SANS) measurements of PEG in solution (pure D<sub>2</sub>O and 3.6 M KCl) show a decreasing radius of gyration confirming this behavior.<sup>59</sup>

The scaling behavior of PEG with ionic strength was tested with four simulations in bulk solution shown in Figure 4. The simulations were performed in pure water and in electrolyte solutions with concentrations of 1 M, 3 M, and 4 M KCl. The results were then compared to simulations of PEG inside the pore. Each point in Figure 4 (black curves) represents 100 ns of simulation data after equilibration of the system. Four properties of PEG, relevant to improving the model, are compared in the figure: the transverse aspect ratio ( $a_{x/y} = x/y$ ), transverse cross-section area ( $A_{\text{PEG}} = (\pi/4) x y$ ), longitudinal length of the molecule ( $L_{\text{PEG}} = z$ ), and the number of cations bound to the chain ( $m_B$ ), Figure 4A–D, respectively. These properties of PEG were calculated by determining the principal components of the molecule in each simulation frame and assigning the longest component to the  $z$ -axis, followed by  $x$  and then  $y$ ; standard errors were calculated by dividing the data into independent blocks that were 10 ns each. Assuming PEG in bulk solution can be represented on average by a cylinder with an elliptical cross-section, the radius of gyration can be expressed in terms of the quantities in Figure 4 as  $R_g^2 = 1/\pi(A_{\text{PEG}}/a_{x/y})(a_{x/y}^2 + 1) + L_{\text{PEG}}^2/12$ . This equation, combined with the trend of  $R_g$  from the experimental data,<sup>59</sup> implies that increasing the electrolyte concentration will cause a decrease in  $a_{x/y}$ ,  $A_{\text{PEG}}$ , and  $L_{\text{PEG}}$  as seen from Figure 4. Furthermore,  $R_g$  calculated from simulations in pure water yields a value of  $15.5 \pm 0.3$  Å, consistent with the SANS results, assuming the polymer acts like a Gaussian coil.<sup>59</sup> The radius of gyration was also calculated for 3.6 M KCl to be  $13.3 \pm 0.5$  Å, by interpolating the curves in Figure 4. This value is  $\sim 10\%$  lower than that measured using SANS data at the same electrolyte concentration, partly because the experimental data were fit

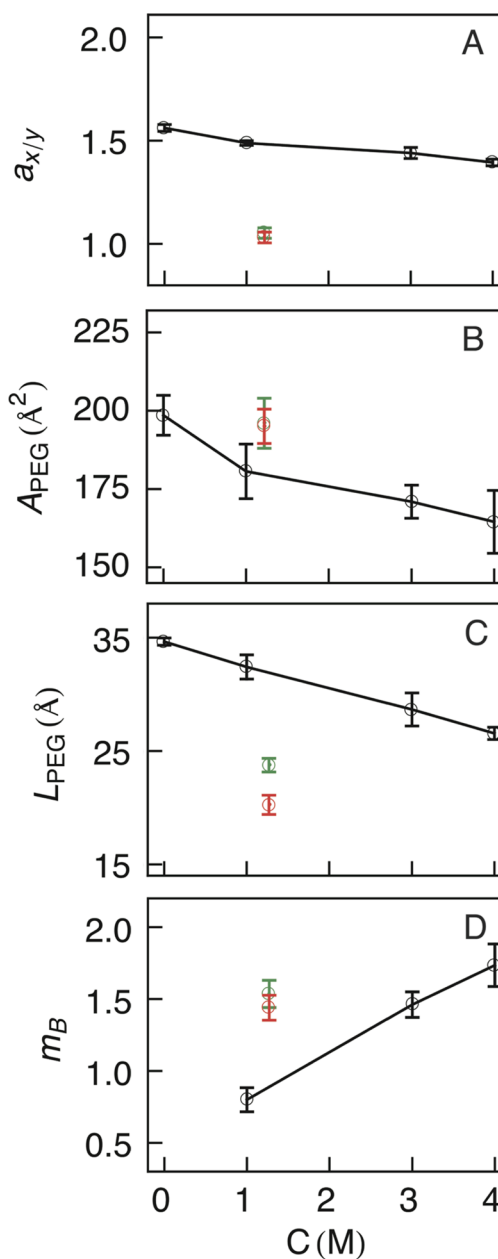


**Figure 4.** Geometric properties of PEG as a function of electrolyte concentration: (A) transverse aspect ratio ( $a_{x/y}$ ); (B) transverse cross-section area ( $A_{\text{PEG}}$ ); (C) longitudinal length ( $L_{\text{PEG}}$ ); (D) number of bound ions ( $m_B$ ). Each property was calculated in the reference frame of the molecule with the longest axis designated as the  $z$ -coordinate, followed by  $x$  and then  $y$ . The plots show properties from simulations of PEG in bulk solution (black curves) and from simulations of PEG inside an  $\alpha$ HL nanopore (conducting regions are shown in green and nonconducting regions in red). Simulation properties for PEG inside the pore are shown at the effective electrolyte concentration in the transmembrane region of 1.27 M KCl (4 M bulk electrolyte concentration).

under the assumption that the molecule acts like an ideal chain<sup>59</sup> and the likely suboptimal parametrization of the CHARMM ion parameters at high electrolyte concentrations.

The electrolyte concentration inside the pore is lower than the bulk value.<sup>52</sup> From the MD trajectories at 4 M KCl, we estimate the salt concentration inside the transmembrane region of the pore to average 30% of the bulk value or  $1.27 \pm$

0.02 M, in the presence of PEG. Inside the pore, PEG conformations have a larger cross-section area and a shorter length than in bulk solution (Figure 4B,C). The conducting (green) and nonconducting states (red) of PEG are plotted at the effective salt concentration inside the pore. From Figure 4A, it is evident that inside the nanopore PEG is more cylindrically symmetric ( $a_{x/y} \approx 1$ ), consistent with the symmetry of the pore.<sup>53</sup> Interestingly, the volume of PEG in bulk solution is qualitatively similar to that inside the pore. However, confinement causes an increase in  $A_{\text{PEG}}$ , relative to simulations in bulk solution, approaching the value in pure water, while  $L_{\text{PEG}}$  is  $\approx 25\%$  smaller. Thus, confinement of PEG in the pore influences its conformation, contrary to previous assertions.<sup>40</sup>

An essential observation from Figure 4 is that inside the pore, the differences in the PEG geometry between the conducting and nonconducting states are small. While  $a_{x/y}$  and  $A_{\text{PEG}}$  are virtually indistinguishable between the two states,  $L_{\text{PEG}}$  decreases by  $\approx 3 \text{ \AA}$  in the nonconducting state, indicating a more compact conformation. In addition to PEG geometry, the conductance is also influenced by the location of the molecule in the channel. The distribution of the PEG center of mass along the pore axis (Figure 5) shows a strong correlation

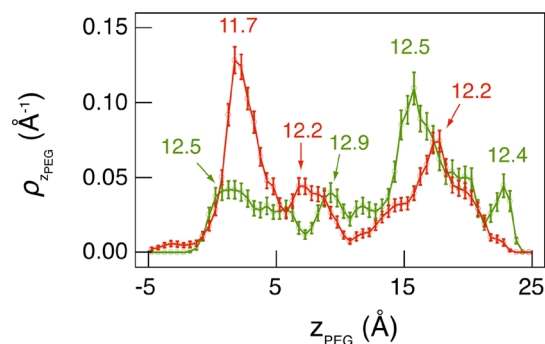


**Figure 5.** Center of mass distribution of PEG inside the pore for conducting (green) and nonconducting states (red). The labels show the radius of the pore ( $R_p$ ) at the location of the individual peaks. The distribution indicates a strong correlation between the channel conductance and pore radius, where the nonconducting states primarily occupy the narrowest regions of the channel.

between channel conductance and pore radius ( $R_p$ ). Deep channel blockades occur predominantly in narrow regions of the pore with  $R_p < 12.4 \text{ \AA}$ . The origin of the two observed states can be further investigated by a more thorough sampling along the pore axis with techniques, such as umbrella sampling<sup>60,61</sup> that will be performed in future work. The fact that the nonconducting state of the channel is correlated with a compact PEG geometry in the narrow regions of the pore (with nonspecific interactions between PEG and the channel) has broad implications in the design of solid-state and hybrid solid-state/biological nanopores.

**Cation Binding.** The coordination of cations by the oxygen atoms in the C–O–C subunit of PEG to form planar crown-ether-like structures has been observed experimentally in the gas phase using ion chromatography<sup>62–65</sup> and to a more limited extent in solution using MD simulations.<sup>58</sup> Simulations performed as part of this work confirm this behavior, as illustrated by the snapshot in Figure 6A. Ion binding was quantified by calculating the radial distribution function ( $g_{\text{K}^+ - \text{PEG}}(r)$ ) between  $\text{K}^+$  ions and the PEG29 oxygen atoms (Figure 6B). The first coordination shell is at  $3.9 \text{ \AA}$ , with no

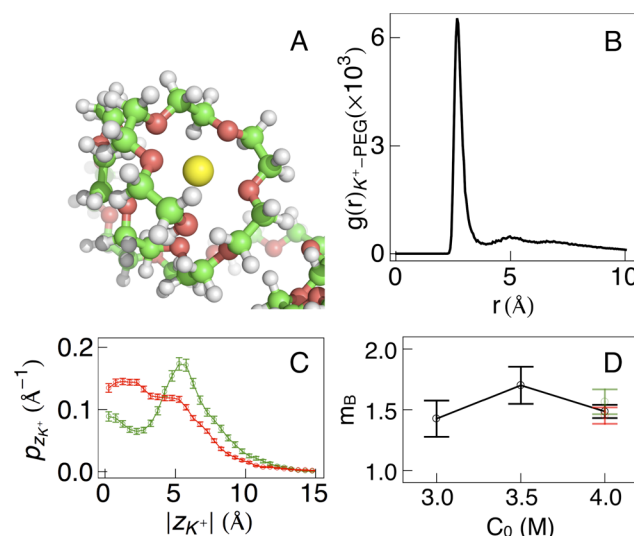


**Figure 6.** PEG coordinates cations in electrolyte solutions. (A) PEG forms planar helical conformations that are analogous to crown ethers. (B) The radial  $\text{K}^+$ –PEG distribution function from simulations of PEG in  $\alpha\text{HL}$  is shown and is used to calculate the coordination number for each cation. (C) The absolute  $z$ -distribution of ions bound to the PEG shows that ions are clustered closer to the center of mass of the molecule in the bound state (red) when compared with the unbound state (green). (D) The number of bound ions does not vary significantly inside the pore for the electrolyte concentrations simulated.

corresponding evidence of coordination between the  $\text{Cl}^-$  ions and PEG (data not shown). The PEG coordination number was calculated by integrating  $g_{\text{K}^+ - \text{PEG}}(r)$  and found to be 4.1 PEG oxygen atoms for each cation.

The preceding result was used for a more detailed analysis of ion binding. For each simulation frame, the number of ions bound to the PEG29 chain was estimated from hydrogen bonding between the cations and PEG oxygen atoms. The cutoff distance was selected to be  $3.9 \text{ \AA}$ , to coincide with the first coordination shell, and an ion was considered bound if it was within the cutoff distance of four or more successive PEG oxygen atoms. In bulk solution, the number of bound cations ( $m_B$ ) scales strongly with electrolyte concentration (Figure 4D). However, inside the pore, the mean number of bound cations for the conducting and nonconducting states is virtually identical ( $1.57 \pm 0.05$  and  $1.47 \pm 0.02$  respectively), with a combined average of  $1.52 \pm 0.03$ . Figure 6C shows the  $z$ -distribution of bound  $\text{K}^+$  ions relative to the center of mass of the PEG inside the nanopore. The denser configurations of PEG in the nonconducting states are further supported by this plot. We observe distinct peaks for each of the two states, with the nonconducting states taking on more compact conformations. Finally, in contrast with simulations of PEG in bulk solution, inside the pore does not change significantly with increasing electrolyte concentration (Figure 6D). From 100 ns trajectories of PEG in  $\alpha\text{HL}$  at 3 and 3.5 M bulk electrolyte concentrations,  $m_B = 1.43 \pm 0.15$  and  $1.70 \pm 0.15$ , respectively.

**Parameter Estimation and Simulation Sampling.** The accurate recovery of ionic currents from simulation trajectories (to benchmark against experiment) requires extensive spatial sampling of the pore and several transitions between the PEG conducting and nonconducting states. The aggregated trajectories of PEG in the nanopore (see Figure 3) only sample  $\approx 20 \text{ \AA}$  of the transmembrane region of the pore and

yield 15 transitions between the conducting and nonconducting states. Therefore, while the simulated ionic currents are statistically consistent with experiment, there is a relatively large uncertainty. The experimentally determined mean residence time of PEG29 in the pore (at 4 M KCl and  $-40$  mV applied potential) is  $\approx 600$   $\mu$ s, which is 2 orders of magnitude longer than the time scales typically accessible with all-atom MD simulations. However, despite the relatively slow convergence of the ionic currents, we are able to estimate the parameters relevant to refining the theoretical model (for example,  $A_{\text{PEG}}$ ,  $L_{\text{PEG}}$ , and  $m_{\text{B}}$ ), which converge on much shorter time scales for the simulations of PEG29 performed here. This is because the difference in these critical model parameters is small between the bound and the unbound states of PEG inside the pore.

**Experimental Data.** Polydisperse PEG distributions (pPEG) with mean molecular weights ( $M_w$ ) of 1000 g/mol and 1500 g/mol were measured experimentally with a single  $\alpha$ HL nanopore incorporated in a DPhyPC lipid bilayer. Data were recorded with bulk electrolyte concentrations of 3 M, 3.5 M, and 4 M KCl and with applied transmembrane potentials between  $-40$  mV and  $-80$  mV relative to the *trans* side of the pore. When no PEG is present in the pore, an average open channel current ( $\langle i_0 \rangle$ ) was recorded that was sensitive to both the applied transmembrane potential and the electrolyte concentration (4 M KCl data shown in Figure 7, left). PEG,

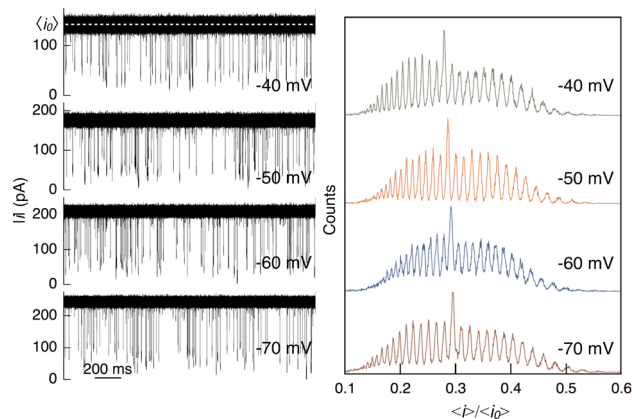


**Figure 7.** Experimental measurements of PEG mixtures (mean molecular weight of 1000 and 1500 g/mol in 4 M KCl at pH 7.2) with a single  $\alpha$ HL nanopore. (Left) Time series of ionic currents are shown at four transmembrane potentials. The mean open channel current ( $\langle i_0 \rangle$ , dashed white, shown at  $-40$  mV) increases with applied potential. PEG partitions into the channel and reduces its conductance ( $\langle i \rangle$ ) proportional to the molecule size. Individual PEG events are then analyzed to estimate the blockade depth ( $\langle i \rangle / \langle i_0 \rangle$ ). (Right) Distribution of  $\langle i \rangle / \langle i_0 \rangle$  at four applied transmembrane potentials. The peaks represent uniquely sized polymers, discriminated with single monomer resolution. A systematic shift of the peaks to the right across the four plots highlight the inverse dependence of  $\langle i \rangle / \langle i_0 \rangle$  with applied potential.

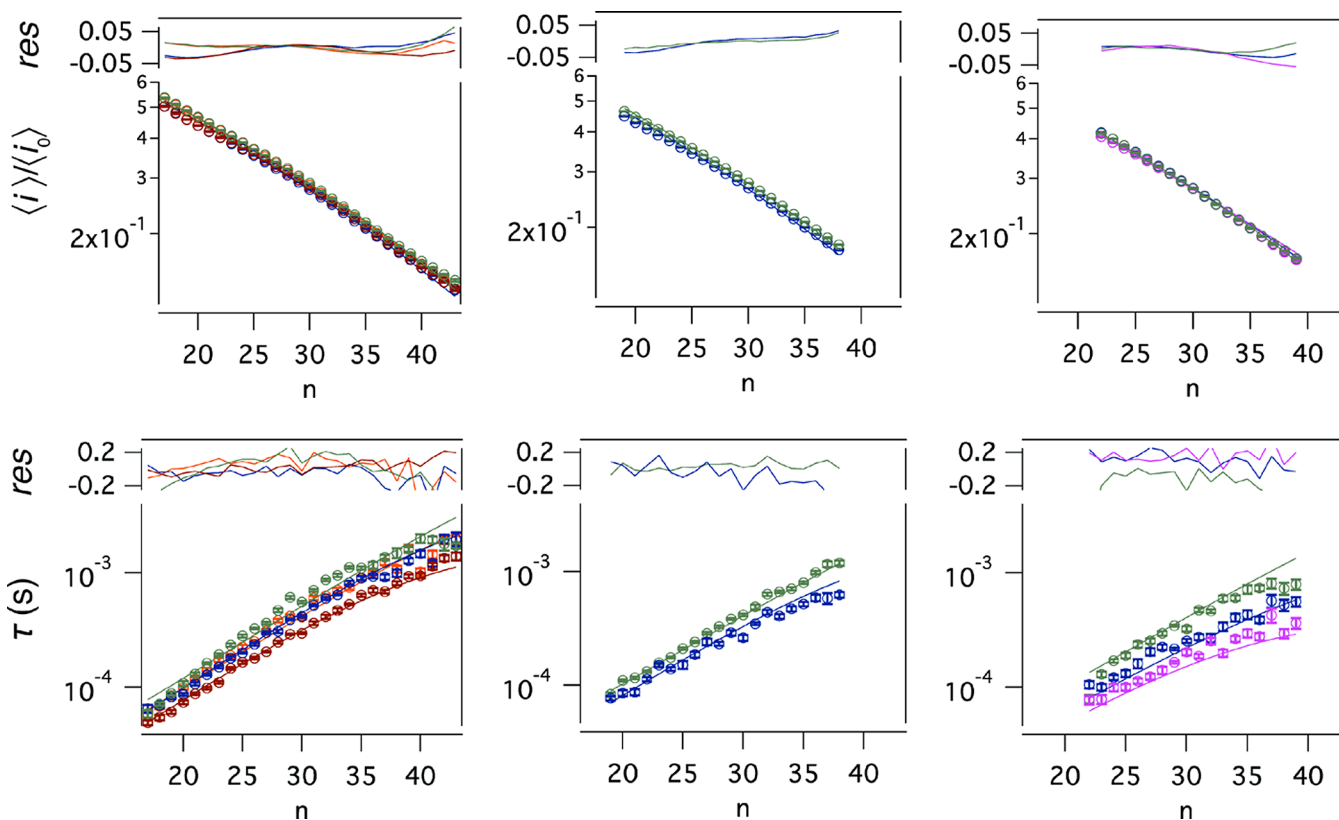
added from the *trans* side of the pore, caused deep, well-defined transient current blockades.<sup>23</sup> A single PEG partitioning into the pore results in an average ionic current ( $\langle i \rangle$ ) that decreases proportional to the size of the molecule. Individual PEG blockade events were analyzed by a thresholding algorithm that determined both the blockade depth ( $\langle i \rangle / \langle i_0 \rangle$ ), by scaling  $\langle i \rangle$  with the average open channel current and the residence time ( $\tau$ ).<sup>24</sup>

Figure 7 (left) shows representative ionic current time-series of pPEG in 4 M KCl (qualitatively similar results were obtained in  $[\text{KCl}] = 3$  and 3.5 M, not shown). The magnitude of the open channel current scaled directly with increasing potential, averaging  $141.2 \pm 0.1$ ,  $176.7 \pm 0.1$ ,  $210.5 \pm 0.2$ , and  $242.9 \pm 0.1$  pA for the applied transmembrane potentials of  $-40$ ,  $-50$ ,  $-60$ , and  $-70$  mV, respectively. The rate of PEG partitioning into the pore was also observed to increase with transmembrane voltage averaging 6.1, 6.2, 7.0, and 8.6 events/s. A histogram of  $\langle i \rangle / \langle i_0 \rangle$  resulted in distinct peaks for each of the four applied transmembrane potentials (Figure 7, right). Each peak in the histogram identifies a single sized PEG molecule with single monomer resolution. The blockade depth distribution was calibrated with an internal standard of highly purified monodisperse PEG29 (1251 g/mol) shown by the tallest peak in each plot. Because  $\langle i \rangle / \langle i_0 \rangle$  scales inversely with the polymer size,<sup>23,24</sup> peaks to the left of PEG29 represent larger polymers. The blockade depth histograms (Figure 7, right) clearly resolve PEG molecules ranging in size from PEG16 (722 g/mol) to PEG40 (1778 g/mol). Furthermore, increasing the transmembrane potentials causes the blockade depth to systematically decrease.<sup>24</sup>

The peak positions in Figure 7 (for the 4 M KCl case) were identified using a peak finder algorithm<sup>24</sup> and then plotted as a function of polymer number in Figure 8. A maximum likelihood estimator was used to assign events to individual peaks in each data set. This allowed a ready estimate of the probability density of residence times as a function of polymer size. The residence times of a given size PEG molecule are exponentially distributed.<sup>23</sup> The mean residence time scales inversely with applied transmembrane potential (Figure 8, bottom).

**Estimation of Model Parameters.** The theoretical model,<sup>24</sup> refined by MD simulations here, was simultaneously fit to the blockade depth and residence time data shown in Figure 8. The blockade depth (eq 1) depends on model parameters, such as the local electrolyte concentration inside the pore in the presence of PEG ( $C_p$ ), the relationship between the electrophoretic and electroosmotic forces acting on cations ( $s^+$ ), the concentration weighted diffusion constants ( $a^*$  and  $b^*$ ), and the free energy of a single cation adsorbing to PEG ( $\Delta G_{\text{pore}}$ ). Because these parameters are invariant with electrolyte concentration and the applied transmembrane potential, they were linked between all data sets in the fit. In addition to the parameters above, the residence time (eq 3) depends on the free energy of confinement ( $\Delta G_c$ ), which was adjusted independently with electrolyte concentration. Equation 3 also depends on parameters that describe the relationship between the electrophoretic and electroosmotic forces acting on PEG ( $s^{\text{PEG}}$ ) and the hydrodynamic drag on the PEG ( $\xi$ ). To reduce the number of free parameters,  $C_p$ ,  $A_{\text{PEG}}$ , and  $L_{\text{PEG}}$  were obtained from MD simulations and therefore fixed in the model. From the simulations, the pore geometry was found to be  $A_{\text{pore}} = 450 \text{ \AA}^2$  and  $L_{\text{pore}} = 49.5 \text{ \AA}$ . Initial values of  $r_m^*$  were obtained from simulations but not fixed in the model.

Blockade depths and residence times as a function of polymer index number ( $n$ ) were simultaneously fit to electrolyte concentrations of 3 M KCl ( $-40$ ,  $-60$ , and  $-80$  mV), 3.5 M KCl ( $-40$  and  $-60$  mV), and 4 M KCl ( $-40$ ,  $-50$ ,  $-60$ , and  $-70$  mV) using the global optimization program Motofit.<sup>66</sup> Figure 8 shows the results of the fits to the blockade depth (left) and residence times (right) in each case, together with the fit residuals. Parameters invariant with electrolyte concentration were found to be  $a^* = 1.553 \pm 0.001$ ,  $b^* = 1.50$



**Figure 8.** Mean blockade depths (top) and residence times (bottom) as a function of the polymer size ( $n$ ) were fit to the refined theoretical model simultaneously. PEG molecules with different sizes were measured experimentally at three electrolyte concentrations: 4 M KCl (first column) at four applied transmembrane potentials of  $-40$  mV (green),  $-50$  mV (orange),  $-60$  mV (blue), and  $-70$  mV (brown); 3.5 M KCl (middle column) at  $-40$  and  $-60$  mV; 3 M KCl (right column) at  $-40$ ,  $-60$ , and  $-80$  mV (magenta). Least squares fits to the data (solid lines) were obtained for the blockade depth,  $\langle i \rangle / \langle i_0 \rangle$  from eq 1 and residence time ( $\tau$ ) from eq 3. Normalized residuals (res) were calculated for each curve using the expression  $1 - \langle i \rangle / \langle i_0 \rangle_{\text{model}} / \langle i \rangle / \langle i_0 \rangle_{\text{data}}$  for the blockade depth and  $1 - \tau_{\text{model}} / \tau_{\text{data}}$  for the residence times.

$\pm 0.02$ ,  $s^+ = 1.39 \pm 0.03$ ,  $s_{\text{PEG}} = 0.108 \pm 0.003$ ,  $\xi = 1172 \pm 16$  Vs/m and  $\Delta G_{\text{pore}} = -5.3 \pm 0.1 k_{\text{B}}T$ . Parameters that vary with the bulk electrolyte concentration ( $C_0$ ) are listed in Table 2. The number of bound ions ( $m_{\text{B}}$ ) for PEG29 is obtained from eq 2 using the estimated fit parameters,  $r_{\text{m}}^+$ ,  $\Delta G_{\text{pore}}$ , and  $s^+$ .

**Table 2. Model Fit Parameters**

$C_0$ , M	$V_{\text{app}}$ , mV	$\Delta G_c$ , $k_{\text{B}}T$	$r_{\text{m}}^+ \times 10^{-3}$	$m_{\text{B}}$ (PEG29)
3.0	$-40$	$0.175 \pm 0.006$	$71.5 \pm 0.3$	$2.01 \pm 0.01$
	$-60$			$1.90 \pm 0.02$
	$-80$			$1.68 \pm 0.03$
3.5	$-40$	$0.175 \pm 0.006$	$69.3 \pm 0.5$	$1.95 \pm 0.01$
	$-60$			$1.85 \pm 0.02$
4.0	$-40$	$0.156 \pm 0.005$	$67.9 \pm 0.3$	$1.91 \pm 0.01$
	$-50$			$1.87 \pm 0.01$
	$-60$			$1.81 \pm 0.01$
	$-70$			$1.72 \pm 0.02$

The refined model of PEG interactions with  $\alpha\text{HL}$  is in excellent agreement with the blockade depth and residence time data (Figure 8). The number of bound ions ( $m_{\text{B}}$ ) was obtained from the simulations (Figure 6D) at  $-40$  mV for each electrolyte concentration in Table 2. Because the simulations were not run for each transmembrane potential,  $m_{\text{B}}$  was not fixed in the model. At 4 M KCl, the model predicts that a

PEG29 binds, on average, three fewer cations than previously reported.<sup>24</sup> Moreover the excellent fit between the experimental data and the model implies that volume exclusion plays a large role in PEG–nanopore interactions. The values of  $m_{\text{B}}$  obtained from the fit are on average 25% higher than those estimated from the simulations at  $-40$  mV (Figure 6D). This is consistent with the systematic error in the simulations due to incorrect parametrization of the force field, including the lack of induced polarization effects. The presence of PEG in the pore drives an electroosmotic flow that opposes the flow of ions.<sup>67</sup> The model estimates these forces through  $s_{\text{PEG}}$ . Assuming PEG is centered in the pore ( $\gamma = 0.5$ ),  $F_{\text{V}}^{\text{PEG}} / F_{\text{E}}^{\text{PEG}} = 0.78 \pm 0.01$ , which agrees with previous experimental studies with PEG<sup>24</sup> and solid-state nanopore DNA experiments.<sup>28,67</sup>

An important consequence of including the effects of cation binding is that the model estimates both the free energy of binding a single cation ( $\Delta G_{\text{pore}}$ ) and the entropic penalty of confining PEG to the pore ( $\Delta G_c$ ). As expected, the value of  $\Delta G_{\text{pore}}$  differs considerably from the binding energies of  $-30 k_{\text{B}}T$  measured experimentally for  $\text{K}^+$ –dimethyl ether (DME) interactions in vacuum.<sup>64</sup> Solvation has a large effect on the binding energy. While direct measurements of the binding energies for the solvated molecule are difficult,  $\Delta G_{\text{pore}}$  is in excellent agreement with  $\text{K}^+$ –DME binding energies calculated in water using quantum mechanical methods.<sup>68</sup> Finally from Table 2,  $\Delta G_c$  is inversely proportional to electrolyte concentration because PEG assumes more compact conformations at higher electrolyte concentration (Figure 4). Interest-

ingly the entropic penalty exceeds the thermal energy at room temperature when  $n > 6$  for all measured electrolyte concentrations. The relatively high entropic penalty will influence the capture rate of PEG by the pore and will need to be considered when designing PEG analogs in applications, such as the proposed nanopore-based DNA sequencing by synthesis.<sup>34</sup>

## CONCLUSIONS

We refined a model of polymer interactions with nanopores using a combination of analytical theory, MD simulations, and new measurements. Predictions made by the simulations are used to test and modify several previous assumptions about the interactions of PEG with the  $\alpha$ HL nanopore. In this study, MD simulations of PEG29 in bulk solution were performed in pure water and with electrolyte concentrations of 1, 3, and 4 M KCl. Additional simulations of PEG29 inside an  $\alpha$ HL nanopore were run with an electrolyte concentration of 4 M KCl and a transmembrane potential of  $-40$  mV. Polydisperse PEG ( $M_w = 1000$  and  $1500$  g/mol) was measured experimentally using an  $\alpha$ HL nanopore with electrolyte concentrations between 3 and 4 M KCl and transmembrane potentials between  $-40$  and  $-80$  mV. Molecular interactions estimated from MD simulations were used to refine the theoretical model, which was then fit to experimental data to yield excellent quantitative agreement for all the measured cases.

The MD simulations predict that the PEG geometry is significantly influenced by the nanopore. Consequently, conformations of PEG obtained from simulations in bulk solution, while qualitatively similar, are not adequate when developing a quantitative model of polymer–nanopore interactions, as had been proposed.<sup>40</sup> The cross-sectional area of PEG29 is  $\sim 20\%$  larger inside the pore, compared with the polymer in bulk solution, and the aspect ratio is commensurate with that of the pore. This is expected, given the lower electrolyte concentration inside the pore and the effects of confinement. The increased cross-sectional area causes volume exclusion to play a greater role in the measured blockade depth, compared with earlier predictions.<sup>24</sup> MD simulations also confirm that PEG binds cations in bulk solution as well as inside the pore. The simulations predict that PEG29 binds  $1.52 \pm 0.02$  cations on average inside the pore (4 M KCl,  $V_{app} = -40$  mV), which is about 3-fold less than that estimated previously.<sup>24,69</sup> An important outcome of using physically accurate parameters obtained from MD simulations is that the free energy of PEG binding a single cation ( $\Delta G_{pore}$ ) is estimated to be  $-5.3 k_B T$ ,  $\sim 2.5$ -fold lower than previously estimated<sup>24</sup> and in quantitative agreement with quantum mechanical calculations.<sup>68</sup> The effect of confinement on PEG geometry was found to be substantial even for relatively small molecules ( $n > 6$ ). This is contrary to the conclusions of previous studies where only molecules with volumes substantially larger than the pore were thought to overcome an entropic barrier at the pore entrance.<sup>70,71</sup> The heights of the entropic barrier per monomer ( $\Delta G_c$ ) for the 3, 3.5 and 4 M KCl data are  $0.175 \pm 0.006$ ,  $0.175 \pm 0.006$ , and  $0.156 \pm 0.005 k_B T$ , respectively.

Finally, the simulations clearly highlight the sensitivity of the ionic currents to the conformation and location of PEG inside the pore. Relatively large differences in the ionic current in the conducting and nonconducting states are the result of subtle differences in PEG conformation, its location in the pore, and ion binding. The microscopic states accessible to MD

simulations are not easily measured experimentally. The combination of the molecular detail from MD simulations with analytical theory makes the tools developed here important when designing either molecular tags for DNA sequencing applications<sup>34</sup> or biological, solid-state, or hybrid nanopores.<sup>72–75</sup>

## AUTHOR INFORMATION

### Corresponding Author

pastorr@nhlbi.nih.gov

### Notes

The authors declare no competing financial interest.

## ACKNOWLEDGMENTS

We thank Wonpil Im and Kyu Il Lee for helpful discussions regarding simulations of ion channels. This work was supported in part by a NRC/NIST-NIH Research Fellowship (A.B.). This research was also supported in part by the Intramural Research Program of the NIH, National Heart, Lung, and Blood Institute, and utilized the high-performance computational capabilities at the National Institutes of Health, Bethesda, MD (NHLBI LoBoS cluster). A.B. thanks the Theoretical and Computational Biophysics Group at the University of Illinois at Urbana–Champaign for training in NAMD. NAMD was developed by the Theoretical and Computational Biophysics Group in the Beckman Institute for Advanced Science and Technology at the University of Illinois at Urbana–Champaign.

## REFERENCES

- (1) Kasianowicz, J. J.; Robertson, J. W. F.; Chan, E. R.; Reiner, J. E.; Stanford, V. M. *Ann. Rev. Anal. Chem.* **2008**, *1*, 737–766.
- (2) Howorka, S.; Siwy, Z. *Chem. Soc. Rev.* **2009**, *38*, 2360–2384.
- (3) Reiner, J. E.; Balijepalli, A.; Robertson, J. W.; Campbell, J.; Suehle, J.; Kasianowicz, J. J. *Chem. Rev.* **2012**, *112*, 6431–6451.
- (4) Song, L.; Hobaugh, M. R.; Shustak, C.; Cheley, S.; Bayley, H.; Gouaux, J. E. *Science* **1996**, *274*, 1859–1866.
- (5) Kasianowicz, J. J.; Bezrukov, S. M. *Biophys. J.* **1995**, *69*, 94–105.
- (6) Bezrukov, S.; Vodyanoy, I.; Brutyan, R.; Kasianowicz, J. *Macromolecules* **1996**, *29*, 8517–8522.
- (7) Bezrukov, S.; Kasianowicz, J. *Phys. Rev. Lett.* **1993**, *70*, 2352–2355.
- (8) Kasianowicz, J.; Brandin, E.; Branton, D.; Deamer, D. *Proc. Natl. Acad. Sci. U.S.A.* **1996**, *93*, 13770–13773.
- (9) Akeson, M.; Branton, D.; Kasianowicz, J. J.; Brandin, E.; Deamer, D. W. *Biophys. J.* **1999**, *77*, 3227.
- (10) Henrickson, S.; Misakian, M.; Robertson, B.; Kasianowicz, J. *Phys. Rev. Lett.* **2000**, *85*, 3057–3060.
- (11) Kasianowicz, J. J. *Nat. Mater.* **2004**, *3*, 355–356.
- (12) Butler, T. Z.; Gundlach, J. H.; Troll, M. *Biophys. J.* **2007**, *93*, 3229–3240.
- (13) Butler, T. Z.; Pavlenok, M.; Derrington, I. M.; Niederweis, M.; Gundlach, J. H. *Proc. Natl. Acad. Sci. U.S.A.* **2008**, *105*, 20647–20652.
- (14) Panwar, A. S.; Muthukumar, M. *J. Am. Chem. Soc.* **2009**, *131*, 18563–18570.
- (15) Halverson, K. M.; Panchal, R. G.; Nguyen, T. L.; Gussio, R.; Little, S. F.; Misakian, M.; Bavari, S.; Kasianowicz, J. J. *J. Biol. Chem.* **2005**, *280*, 34056–34062.
- (16) Karginov, V. A.; Nestorovich, E. M.; Yohannes, A.; Robinson, T. M.; Fahmi, N. E.; Schmidtman, F.; Hecht, S. M.; Bezrukov, S. M. *Antimicrob. Agents Chemother.* **2006**, *50*, 3740–3753.
- (17) Oukhaled, G.; Mathé, J.; Bianche, A. L.; Bacri, L.; Betton, J. M.; Lairez, D.; Pelta, J.; Auvray, L. *Phys. Rev. Lett.* **2007**, *98*, 158101.
- (18) Cressiot, B.; Oukhaled, A.; Patriarche, G.; Pastoriza-Gallego, M.; Betton, J.-M.; Auvray, L.; Muthukumar, M.; Bacri, L.; Pelta, J. *ACS Nano* **2012**, *6*, 6236–6243.

- (19) Movileanu, L.; Schmittschmitt, J. P.; Scholtz, J. M.; Bayley, H. *Biophys. J.* **2005**, *89*, 1030–1045.
- (20) Bezrukov, S.; Kasianowicz, J. *Eur. Biophys. J.* **1997**, *26*, 471–476.
- (21) Bezrukov, S. M. *J. Membr. Biol.* **2000**, *174*, 1–13.
- (22) Bezrukov, S. M.; Krasilnikov, O. V.; Yuldasheva, L. N.; Berezhkovskii, A. M.; Rodrigues, C. G. *Biophys. J.* **2004**, *87*, 3162–3171.
- (23) Robertson, J. W. F.; Rodrigues, C. G.; Stanford, V. M.; Rubinson, K. A.; Krasilnikov, O. V.; Kasianowicz, J. *J. Proc. Natl. Acad. Sci. U.S.A.* **2007**, *104*, 8207–8211.
- (24) Reiner, J. E.; Kasianowicz, J. J.; Nablo, B. J.; Robertson, J. W. F. *Proc. Natl. Acad. Sci. U.S.A.* **2010**, *107*, 12080–12085.
- (25) Movileanu, L.; Bayley, H. *Proc. Natl. Acad. Sci. U.S.A.* **2001**, *98*, 10137–10141.
- (26) Murphy, R. J.; Muthukumar, M. *J. Chem. Phys.* **2007**, *126*, 051101.
- (27) Gibrat, G.; Pastoriza-Gallego, M.; Thiebot, B.; Breton, M.-F.; Auvray, L.; Pelta, J. *J. Phys. Chem. B* **2008**, *112*, 14687–14691.
- (28) Keyser, U. F.; Kooleman, B. N.; Van Dorp, S.; Krapf, D.; Smeets, R. M. M.; Lemay, S. G.; Dekker, N. H.; Dekker, C. *Nat. Phys.* **2006**, *2*, 473–477.
- (29) Van Dorp, S.; Keyser, U. F.; Dekker, N. H.; Dekker, C.; Lemay, S. G. *Nat. Phys.* **2009**, *5*, 347–351.
- (30) Manrao, E. A.; Derrington, I. M.; Pavlenok, M.; Niederweis, M.; Gundlach, J. H. *PLoS ONE* **2011**, *6*, e25723.
- (31) Cherf, G. M.; Lieberman, K. R.; Rashid, H.; Lam, C. E.; Karplus, K.; Akeson, M. *Nat. Biotechnol.* **2012**, *30*, 344–348.
- (32) Manrao, E. A.; Derrington, I. M.; Laszlo, A. H.; Langford, K. W.; Hopper, M. K.; Gillgren, N.; Pavlenok, M.; Niederweis, M.; Gundlach, J. H. *Nat. Biotechnol.* **2012**, *30*, 349–353.
- (33) Clarke, J.; Wu, H.-C.; Jayasinghe, L.; Patel, A.; Reid, S.; Bayley, H. *Nat. Nanotechnol.* **2009**, *4*, 265–270.
- (34) Kumar, S.; Tao, C.; Chien, M.; Hellner, B.; Balijepalli, A.; Robertson, J. W. F.; Li, Z.; Russo, J. J.; Reiner, J. E.; Kasianowicz, J. J.; Ju, J. *Sci. Rep.* **2012**, *2*, 684.
- (35) The PyMOL Molecular Graphics System, version 1.3r1; Schrödinger, LLC: Cambridge, MA, 2010.
- (36) Phillips, J. C.; Braun, R.; Wang, W.; Gumbart, J.; Tajkhorshid, E.; Villa, E.; Chipot, C.; Skeel, R. D.; Kalé, L.; Schulten, K. *J. Comput. Chem.* **2005**, *26*, 1781–1802.
- (37) Brooks, B. R.; Brucoleri, R. E.; Olafson, B. D.; Swaminathan, S.; Karplus, M. *J. Comput. Chem.* **1983**, *4*, 187–217.
- (38) MacKerell, A. D., Jr; Bashford, D.; Bellott, M.; Dunbrack, R. L., Jr; Evanseck, J. D.; Field, M. J.; Fischer, S.; Gao, J.; Guo, H.; Ha, S. *J. Phys. Chem. B* **1998**, *102*, 3586–3616.
- (39) MacKerell, A. D.; Feig, M.; Brooks, C. L. *J. Comput. Chem.* **2004**, *25*, 1400–1415.
- (40) Lee, H.; Venable, R. M.; MacKerell, A. D. J.; Pastor, R. W. *Biophys. J.* **2008**, *95*, 1590–1599.
- (41) Klauda, J. B.; Venable, R. M.; Freites, J. A.; O'Connor, J. W.; Tobias, D. J.; Mondragon-Ramirez, C.; Vorobyov, I.; MacKerell, A. D.; Pastor, R. W. *J. Phys. Chem. B* **2010**, *114*, 7830–7843.
- (42) Jorgensen, W. L.; Chandrasekhar, J.; Madura, J. D.; Impey, R. W.; Klein, M. L. *J. Chem. Phys.* **1983**, *79*, 926.
- (43) Martyna, G. J.; Tobias, D. J.; Klein, M. L. *J. Chem. Phys.* **1994**, *101*, 4177.
- (44) Feller, S. E.; Zhang, Y. H.; Pastor, R. W.; Brooks, B. R. *J. Chem. Phys.* **1995**, *103*, 4613–4621.
- (45) Darden, T.; York, D.; Pedersen, L. *J. Chem. Phys.* **1993**, *98*, 10089.
- (46) Ryckaert, J.-P.; Ciccotti, G.; Berendsen, H. J. C. *J. Comput. Phys.* **1977**, *23*, 327–341.
- (47) Jo, S.; Kim, T.; Iyer, V. G.; Im, W. *J. Comput. Chem.* **2008**, *29*, 1859–1865.
- (48) White, R. J.; Ervin, E. N.; Yang, T.; Chen, X.; Daniel, S.; Cremer, P. S.; White, H. S. *J. Am. Chem. Soc.* **2007**, *129*, 11766–11775.
- (49) Misakian, M.; Kasianowicz, J. *J. Membr. Biol.* **2003**, *195*, 137–146.
- (50) Robertson, J. W. F.; Kasianowicz, J. J.; Reiner, J. E. *J. Phys.: Condens. Matter* **2010**, *22*, 454108.
- (51) Pezeshki, S.; Chimere, C.; Bessonov, A. N.; Winterhalter, M.; Kleinekathöfer, U. *Biophys. J.* **2009**, *97*, 1898–1906.
- (52) Noskov, S. Y.; Im, W.; Roux, B. *Biophys. J.* **2004**, *87*, 2299–2309.
- (53) Aksimentiev, A.; Schulten, K. *Biophys. J.* **2005**, *88*, 3745–3761.
- (54) Rui, H.; Lee, I., K.; Pastor, R. W.; Im, W. *Biophys. J.* **2011**, *100*, 602–610.
- (55) Lee, K. I.; Jo, S.; Rui, H.; Egwolf, B.; Roux, B.; Pastor, R. W.; Im, W. *J. Comput. Chem.* **2012**, *33*, 331–339.
- (56) Doi, M.; Edwards, S. F. *The Theory of Polymer Dynamics*; Oxford University Press: Oxford, 1988.
- (57) Thiyagarajan, P.; Chaiko, D. J.; Hjelm, R. P., Jr *Macromolecules* **1995**, *28*, 7730–7736.
- (58) Tasaki, K. *Comput. Theor. Polym. Sci.* **1999**, *9*, 271–284.
- (59) Rubinson, K. A.; Krueger, S. *Polymer* **2009**, *50*, 4852–4858.
- (60) Torrie, G. M.; Valleau, J. P. *J. Comput. Phys.* **1977**, *23*, 187–199.
- (61) Kumar, S.; Rosenberg, J. M.; Bouzida, D.; Swendsen, R. H.; Kollman, P. A. *J. Comput. Chem.* **1992**, *13*, 1011–1021.
- (62) Helden, von, G.; Wyttenbach, T.; Bowers, M. T. *Int. J. Mass Spectrom.* **1995**, *146*, 349–364.
- (63) Helden, von, G.; Wyttenbach, T.; Bowers, M. T. *Science* **1995**, *267*, 1483–1485.
- (64) More, M. B.; Ray, D.; Armentrout, P. B. *J. Phys. Chem. A* **1997**, *101*, 831–839.
- (65) Wyttenbach, T.; Helden, von, G.; Bowers, M. T. *Int. J. Mass Spectrom.* **1997**, *165*, 377–390.
- (66) Nelson, A. *J. Appl. Crystallogr.* **2006**, *39*, 273–276.
- (67) Ghosal, S. *Phys. Rev. Lett.* **2007**, *98*, 238104.
- (68) Thompson, M. A.; Glendenning, E. D.; Feller, D. *J. Phys. Chem* **1994**, *98*, 10465–10476.
- (69) Kasianowicz, J. J.; Reiner, J. E.; Robertson, J. W. F.; Henrickson, S. E.; Krasilnikov, O. V. In *Nanopore-based Technology*; Gracheva, M. E., Ed.; Humana Press: Totowa, New Jersey, 2012; Vol. 870, p 267.
- (70) Krasilnikov, O. V.; Rodrigues, C. G.; Bezrukov, S. M. *Phys. Rev. Lett.* **2006**, *97*, 018301.
- (71) Rodrigues, C. G.; Machado, D. C.; Chevchenko, S. F.; Krasilnikov, O. V. *Biophys. J.* **2008**, *95*, 5186–5192.
- (72) Stoddart, D.; Heron, A. J.; Mikhailova, E.; Maglia, G.; Bayley, H. *Proc. Natl. Acad. Sci. U.S.A.* **2009**, *106*, 7702–7707.
- (73) Langecker, M.; Arnaut, V.; Martin, T. G.; List, J.; Renner, S.; Mayer, M.; Dietz, H.; Simmel, F. C. *Science* **2012**, *338*, 932–936.
- (74) Russo, C. J.; Golovchenko, J. A. *Proc. Natl. Acad. Sci. U.S.A.* **2012**, *109*, 5953–5957.
- (75) Kuan, A. T.; Golovchenko, J. A. *Appl. Phys. Lett.* **2012**, *100*, 213104–2131044.